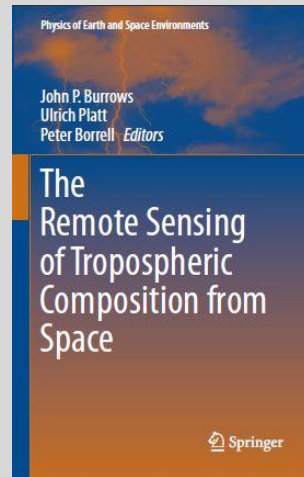


# **The Remote Sensing of Tropospheric Composition from Space**

Editors:

John P. Burrows  
Ulrich Platt  
Peter Borrell

*Pages 231 to 258*



## **Chapter 5**

### **Remote Sensing of Terrestrial Clouds from Space using Backscattering and Thermal Emission Techniques**

Alexander A. Kokhanovsky, Steven Platnick and  
Michael D. King

Publisher: Springer Verlag, Heidelberg

[Springer Book Web Page](#)

[Springer on line Page for the Book](#)

ISBN 978-3-642-14790-6

DOI 10.1007/978-3-642-14791-3

**February 2011**



# Chapter 5

## Remote Sensing of Terrestrial Clouds from Space using Backscattering and Thermal Emission Techniques

Alexander A. Kokhanovsky, Steven Platnick and Michael D. King

### 5.1 Introduction

Clouds play an important role in terrestrial atmospheric dynamics, thermodynamics, chemistry, and radiative transfer and are key elements of the water and energy cycles. Cloud properties can be modified by anthropogenic and natural gaseous and aerosol emissions (i.e. aerosol indirect effect) and are important for understanding climate change. Therefore, it is of a great importance to understand cloud characteristics and their distributions on a global scale. This can only be achieved using satellite observations.

The first picture of cloud fields from space was recorded after the launch of the unmanned V-2 rocket designed by W. von Braun (USA, 1946) followed by TV images from the low Earth orbit Television Infrared Observation Satellites (e.g. TIROS-1, 1st April 1960). The first visual observations of cloud fields from space were reported by the first cosmonaut, Y. A. Gagarin, who orbited the Earth on the Vostok spacecraft (12th April 1961). Photo, video, and hand-held spectrometry of cloud fields from numerous manned Soviet and American spacecraft soon followed.

However, the era of quantitative long-term cloud observations from space began only 30 years ago with the launch of the first TIROS-N satellite (13th October, 1978). This was an experimental satellite developed by NASA and operated by NOAA. It carried a 4-channel Advanced Very High Resolution Radiometer (AVHRR) to provide day and night cloud top and sea surface temperatures, as well as ice and snow conditions; an atmospheric sounding system (TOVS–TIROS Operational Vertical Sounder) to provide profiles of temperature and water vapour from the Earth's surface to the top of the atmosphere. Since then, many imaging

---

A.A. Kokhanovsky (✉)

Institute of Environmental Physics, University of Bremen, Germany

S. Platnick

NASA Goddard Space Flight Center, Greenbelt, MD, USA

M.D. King

Laboratory for Atmospheric and Space Physics, University of Colorado, Boulder, CO 80309, USA

radiometers and spectrometers have been launched. Collectively, they provide a comprehensive global picture for a range of cloud properties and their spatial distributions. The characteristics of selected passive optical instruments currently in operation and their derived cloud products are summarized in Appendix A.

The main cloud products derived from passive optical satellite observations are:

- Cloud cover,
- Cloud thermodynamic phase,
- Cloud optical thickness,
- Cloud droplet/crystal effective radius,
- Cloud liquid/ice water path, and
- Cloud top properties (temperature, pressure/height).

Recent satellite-borne lidar and radar systems reveal the internal structure of cloud systems on a level of detail not possible with passive optical measurements.

The structure of this chapter is as follows: in Section 5.2 we define the main cloud parameters derived from optical satellite measurements. The corresponding algorithms are outlined and results of retrievals are given. The following section has a focus on the description of cloud validation experiments and satellite cloud retrieval uncertainties. In the last section the modern trends in cloud remote sensing and selected planned satellite missions are reviewed.

## 5.2 Cloud Parameters and Their Retrievals

On average, about 70% of the Earth's surface is covered by clouds. The cloud fraction is a very important parameter, e.g. for the climate studies and also for the retrievals of the vertical columns of trace gases using space-borne instrumentation. It is equal to the ratio of the area of a pixel covered by a cloud to the total area. Other macroscopic characteristics such as the cloud top height, the cloud geometrical thickness, the cloud base height and the number of cloud layers are of interest as well. The cloud top height is important, e.g. for the correction of column trace gas retrieval algorithms in the presence of clouds. The cloud characteristics must be determined with the highest possible accuracy for the creation of reliable bias-free trace gas vertical columns products and databases.

Microphysical parameters, e.g. the cloud particle number density  $N$ , phase (liquid or solid) of cloud particles, size/shape distributions of cloud particles and their refractive index are used to calculate cloud local optical characteristics, which are the cloud extinction  $k_{ext}$  and absorption  $k_{abs}$  coefficients, single scattering albedo  $\omega_0 = 1 - k_{abs}/k_{ext}$ , and the phase matrix. The extinction and absorption coefficients can be calculated from the following equations:  $k_{ext} = N\langle C_{ext} \rangle$ ,  $k_{abs} = N\langle C_{abs} \rangle$ . Here  $\langle C_{ext} \rangle$  and  $\langle C_{sca} \rangle$  are corresponding average extinction and absorption cross sections of scatterers in a cloud (Liou 2002).

For an idealized vertically homogeneous cloud, the cloud optical thickness  $\tau$  is defined as:  $\tau = k_{ext}L$ , where  $L$  is the cloud geometrical thickness. For oriented crystals, the extinction matrix must also be calculated.

The global cloud characteristics such as the Stokes vector of the reflected, transmitted and internal light fields can be found from the solution of the vector radiative transfer equation (Liou 2002). The first component of the Stokes vector  $I^\uparrow$  can be used to find the cloud reflectance  $R = \pi I^\uparrow / \mu_0 F_0$ , where  $\mu_0$  is the cosine of the solar zenith angle,  $F_0$  is the solar irradiance at the top of atmosphere. Modern satellite instrumentation is capable of measuring  $I^\uparrow$ ,  $F_0$  and, therefore, cloud reflectance can easily be derived and used for the interpretation of measurements and the development of retrieval algorithms.

### 5.2.1 Cloud Cover

Cloud cover or cloud fraction, both terms are used, is defined as the fraction of a given scene covered by cloud, and so ranges from zero for clear skies to unity for overcast scenes. While simple in concept, it is inherently an ill-defined quantity that depends on the spectral region being considered, the spatial resolution of the imager, and the intended application (Schreiner et al. 1993; Ackerman et al. 1998; Wylie et al. 2005). Cloud cover is often derived from algorithms that attempt to identify fields of view contaminated by cloud as part of the pre-processing when determining surface and aerosol optical properties. A cloud mask results from such algorithms. Cloud cover determined from masking approaches is influenced by the spatial resolution of the instrument. Provided the signal to noise ratio of the instrument is sufficient, then smaller errors are achieved on data products for instruments with higher spatial resolution. The instrument spectral and signal-to-noise capabilities are also of great significance as they determine the ability to observe the cloud. For example, a thin cirrus cloud, detectable in a sensitive water vapour absorption band, may not be detectable in the visible. Cloud cover results are also sensitive to algorithm approaches.

Both solar reflectance in daytime observations, and thermal emission bands are used to discriminate cloudy from clear-sky scenes. The identification of cloudy scenes by discrimination of the intensity of backscattered solar radiation is often challenging, for example, as a result of bright underlying surfaces such as snow and desert for solar reflectance bands. A global cloud cover product is often aggregated from individual scenes to a global grid, e.g. such as a  $1^\circ \times 1^\circ$  equal-angle grid for Moderate Resolution Imaging Spectroradiometer, MODIS, products from the NASA Earth Observing System Aqua and Terra satellites. In addition to global maps, cloud cover is often shown as a zonal mean (averaged over discrete latitudinal belts), and separately for ice and liquid water clouds. The cloud fraction derived from a monthly aggregation of the MODIS cloud mask product (product identification MYD35 for MODIS Aqua) is shown in Fig. 5.1 for April 2005.

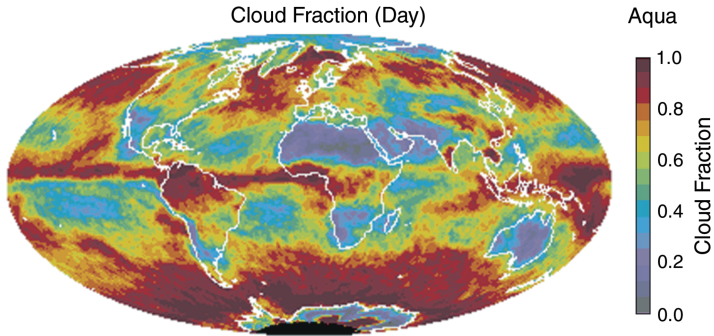


**Fig. 5.1** Monthly cloud fraction (daytime observations) derived from the MODIS Aqua cloud mask for April 2005.

Night-time cloud fractions are nearly indistinguishable from those shown in Fig. 5.1. Overall the greatest cloud occurrences are found over oceans, especially in the southern oceans around Antarctica. The mean latitudinal behavior of this cloud fraction is given in Fig. 5.2. The distribution of cloud fraction depends on the underlying surface type.

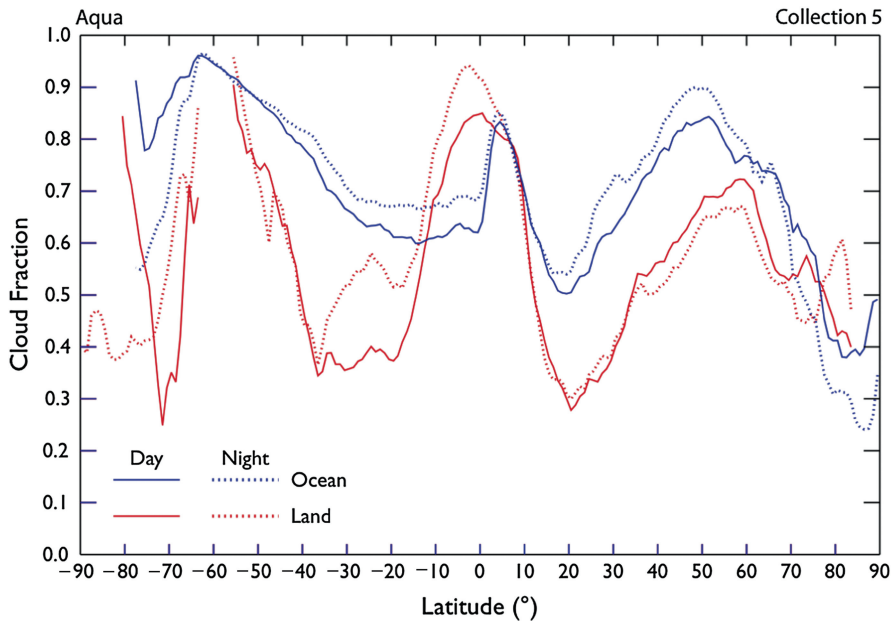


**Fig. 5.2** Zonal mean monthly cloud fraction (daytime and night-time observations) derived from the MODIS Aqua cloud mask for April 2005.

### 5.2.2 Cloud Phase

A phase index  $P = R(1550 \text{ nm})/R(1670 \text{ nm})$  (the numbers refer to the wavelengths), which uses the reflectance ratio within the liquid and ice absorption bands, is applied for the discrimination of liquid water and ice clouds when the spectral resolved measurements are available (Knap et al. 2002; Kokhanovsky et al. 2006). Liquid water and ice have different absorptions at these wavelengths. For liquid water clouds, reflectances at 1550 and 1670 nm are similar but those for ice differ, where  $R(1550 \text{ nm}) \leq P_t R(1670 \text{ nm})$ . The threshold value (THV) of the phase index  $P_t = 0.7$  is often used to discriminate ice clouds. Calculations and measurements show that  $P$  is usually above 0.8 for liquid water clouds.

Mixed phase clouds have intermediate values of  $P$ . They can be identified using a  $P$ - $T$  diagram, where the cloud brightness temperature at  $12 \mu\text{m}$  ( $BT_{12}$ ) is plotted along the abscissa and the phase index is plotted along the ordinate axis. The example shown in Fig. 5.3 was created using the SCIAMACHY phase index and AATSR brightness temperature measurements. The collocated measurements of AATSR and SCIAMACHY over Hurricane Isabel (17th September 2003;  $30^\circ\text{N}$ ,  $72^\circ\text{W}$ ) were used in the preparation of data shown in Fig. 5.3. Liquid water clouds are separated by the region where  $BT_{12}$  is above  $273\text{K}$  and the phase index is above 0.8. Values of the phase index between 0.7 and 0.8 are assigned to mixed phase clouds; clouds with  $P > 0.8$  and  $BT_{12} < 273\text{K}$  correspond to super-cooled water. The FTS instrument on GOSAT, which was launched by JAXA in January 2009, measures simultaneously  $P$  and  $BT_{12}$  ([http://www.jaxa.jp/press/009/02/20090209\\_ibuki\\_e.html](http://www.jaxa.jp/press/009/02/20090209_ibuki_e.html)). Therefore, corresponding dataset is useful for studies of mixed clouds and also for the detection of super-cooled water.

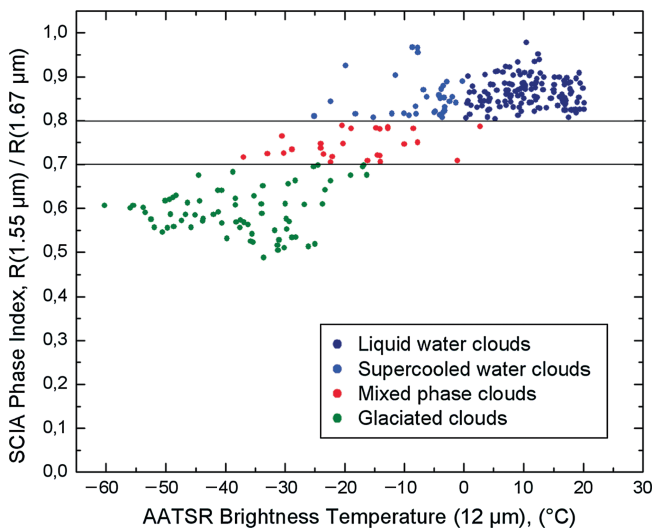
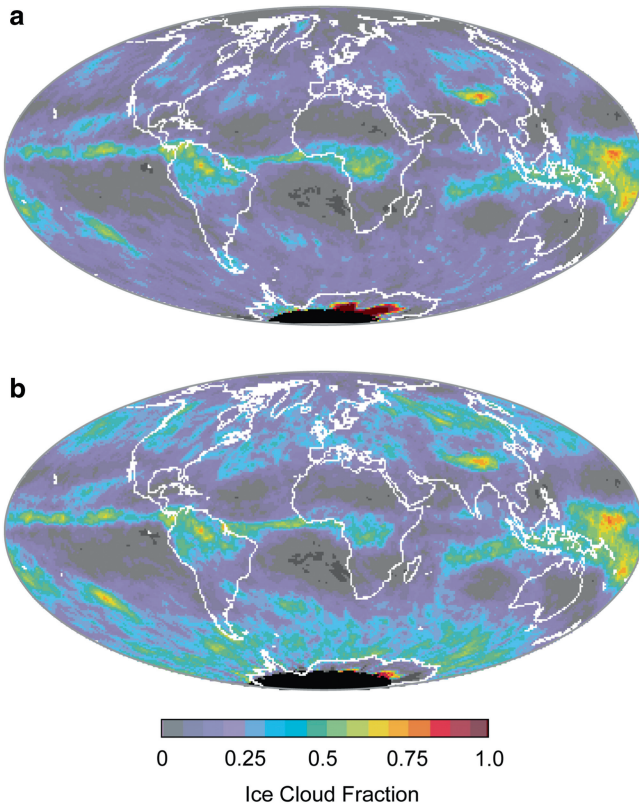


Fig. 5.3 Thermodynamic phase versus brightness temperature ( $P$ - $T$ ) diagram (Kokhanovsky et al. 2006).

The MODIS instrument measures infrared and solar reflectances, which are used to retrieve the cloud phase (Pilewskie and Twomey 1987; Baum et al. 2000). The IR bi-spectral method relies on a number of THVs for the 8.5 and 11  $\mu\text{m}$  brightness temperatures. In addition, measurements around 1.38, 1.6, and 2.1  $\mu\text{m}$  are used to refine the cloud phase algorithm for use in cloud optical property retrievals. A monthly example of this bi-spectral infrared phase result is shown in Fig. 5.4a. The algorithm distinguishes ice clouds in the Inter-Tropical Convergence Zone (ITCZ) and central Pacific regions, though it probably misclassifies ice clouds and snow/ice on the ground in Antarctica. The cloud retrieval phase algorithm, that also includes near-infrared measurements (Fig. 5.4b), gives somewhat larger ice cloud fractions, especially in the extensive cloud layer surrounding Antarctica (the roaring 40s) and in the continental storm tracks over land in the northern hemisphere.



**Fig. 5.4** Mean monthly ice cloud fraction for April 2005 derived from the MODIS bi-spectral infrared algorithm (a), and the cloud optical property retrieval algorithm (b).

Another approach to determine cloud phase is based on using polarization information about the scattered upwelling radiation over a range of scattering angles, where spherical and non-spherical polarised phase functions are distinct

(Goloub et al. 2000). The CNES POLDER instrument (flown on the JAXA ADEOS and ADEOS-II/MIDORI platforms, and currently on PARASOL) provides such capability. Synergistic data products derived from algorithms combining polarized and total radiance/reflectance measurements made by the instruments in the A-Train afternoon constellation of Earth observing satellites, which include POLDER/PARASOL and MODIS/Aqua, are currently being explored.

Multilayer/multiphase cloud scenes are challenging for passive measurements because a single unambiguous phase does not describe the scene well. Approaches for flagging such scenes are being explored by a number of investigators; a scene-level multilayer cloud flag is provided in the Collection 5 MODIS cloud products.

### 5.2.3 Cloud Optical Thickness

Cloud optical thickness,  $\tau$ , together with the cloud fraction  $c$ , has a significant impact on the transfer of solar and infrared radiation through a cloudy atmosphere.  $\tau$  is defined as the cloud extinction coefficient  $k_{\text{ext}}$  integrated across the cloud vertical extent. In the framework of the independent pixel approximation, the albedo for a particular scene averaged over all solar incident angles is given as:

$$r = (1 - c)r_{\text{clear}} + cr_{\text{cloud}}, \quad (5.1)$$

where  $r_{\text{clear}}$  is the spherical albedo for the clear sky portion and  $r_{\text{cloud}}$  is the same quantity for the cloudy scene.

For a clear atmosphere over land,  $r_{\text{clear}}$  in the visible and near-infrared is determined mainly by the surface contribution, which is highly variable with respect to wavelength, season, and surface type and location. Over oceans and outside the sun glint region, the contribution from the atmosphere becomes more important due to the low ocean reflectance.

The value of  $r_{\text{cloud}}$  not only depends on the cloud optical thickness, but also on the particle asymmetry parameter,  $g$ , defined as

$$g = \frac{1}{2} \int_0^\pi p(\theta) \sin \theta \cos \theta d\theta, \quad (5.2)$$

where the phase function  $p(\theta)$  describes the angular distribution of light scattered by a unit cloud volume. The following approximation is used to estimate the cloud spherical albedo in the visible, where the processes of light absorption by liquid water or ice in clouds can be neglected (Kokhanovsky 2006):

$$r_{\text{cloud}} = 1 - t_{\text{cloud}}, \quad t_{\text{cloud}} = \frac{1}{a + b\tau}. \quad (5.3)$$

Here  $t_{\text{cloud}}$  is the cloud spherical transmittance,  $a = 1.07$  and  $b = 0.75(1-g)$ .

It follows from Eq. 5.3 that larger values of  $g$  lead to larger values of light transmission through a cloud, and correspondingly to a smaller reflectance. Ice cloud particles are thought to have values of  $g$  around 0.75 or somewhat higher, and liquid water cloud droplets are characterized by  $g = 0.85$  across the typical range of effective radii. Therefore, liquid water clouds having the same optical thickness as that of ice clouds are generally less reflective; i.e. there is more transmitted light. Eq. 5.3 can be used for the estimation of the cloud albedo if the value of  $\tau$  is retrieved from satellite data.

For optically thick clouds, the optical thickness in the visible is estimated from the following equation (Rozenberg et al. 1978; King 1987; Kokhanovsky et al. 2003) for the cloud reflectance:

$$R(\mu, \mu_0, \varphi) = R_{0\infty}(\mu, \mu_0, \varphi) - t_{cloud}K_0(\mu)K_0(\mu_0). \quad (5.4)$$

Here  $\mu$  is the cosine of the observation zenith angle,  $\mu_0$  is the cosine of the solar zenith angle and  $\varphi$  is the relative azimuth. All functions in Eq. 5.4 (except  $K_0$ ) depend on  $\tau$ .

Assuming a given cloud model, e.g. spherical particles and a polydisperse distribution with a given effective radius of droplets,  $a_{ef}$ , or predefined ice crystals shapes and size distributions, the escape function  $K_0(\mu)$ , and the reflection function for a semi-infinite non-absorbing layer  $R_{0\infty}$  are pre-calculated and stored in look-up-tables (LUTs). Approximate equations for these functions can be used as well. In particular, a good approximation for  $K_0(\mu)$  is:

$$K_0(\mu) = \frac{3}{7}(1 + 2\mu). \quad (5.5)$$

This function describes the angular distribution of the radiation escaping a semi-infinite non-absorbing turbid medium with sources located at the infinite depth in the medium. Due to strong multiple scattering effects, its dependence on the microphysical properties of the medium can be neglected.

One derives from Eq. 5.3 and Eq. 5.4:

$$\tau = \frac{1}{b} \left[ \frac{K_0(\mu)K_0(\mu_0)}{R_{0\infty}(\mu, \mu_0, \varphi) - R(\mu, \mu_0, \varphi)} - a \right]. \quad (5.6)$$

It follows from this equation that retrievals of  $\tau$  for very thick clouds ( $R \rightarrow R_{\infty}$ ) are highly uncertain and small errors, e.g. calibration errors, in the measured reflection function will lead to large errors in the retrieved cloud optical thickness. Often, a limiting value of cloud optical thickness is used in the retrieval process, e.g. 100, as most clouds, but certainly not all, have optical thicknesses below 100.

The mean retrieved MODIS Aqua cloud optical thickness (liquid and ice phase) for April 2005 is shown in Fig. 5.5 (aggregated from the MYD06 pixel-level product). One can see that clouds are optically thin in subsidence regions outside the ITCZ along with low cloud fraction (Fig. 5.2). Having lost most of its water vapour to condensation and rain in the upward branch of the circulation, the

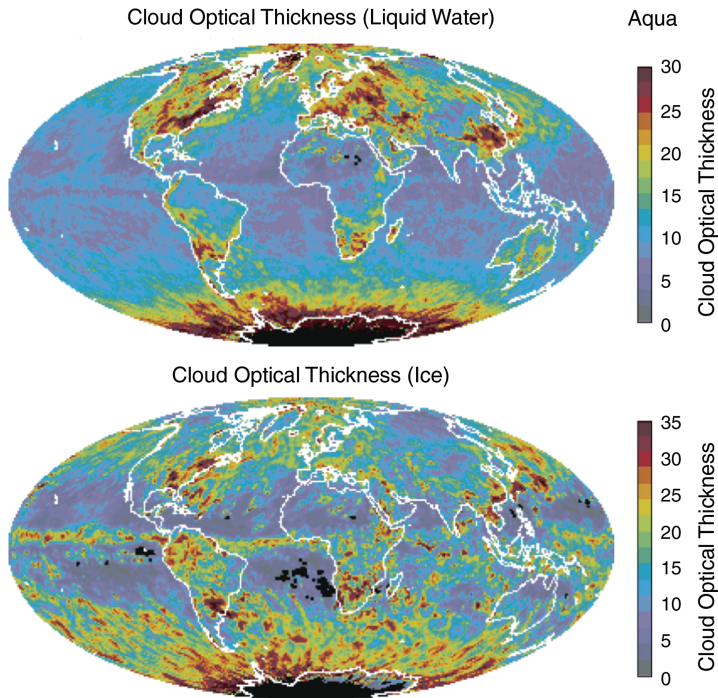


**Fig. 5.5** Monthly cloud optical thicknesses derived from the MODIS Aqua cloud optical properties product for April 2005.

descending air is dry in these regions. The corresponding latitudinal variation in the mean cloud optical thickness is shown in Fig. 5.6. One can see that ice clouds are thicker in the ITCZ zone. Thin clouds, defined as having  $\tau < 5$  are almost absent in the latitudinal averages shown in Fig. 5.6. There are no latitudinal belts with cloud fraction less than 0.2 (see Fig. 5.2).

It follows from Eq. 5.6 that the retrievals of the product  $b\tau$  and, therefore,  $r_{\text{cloud}}$  is less influenced by the assumptions on the asymmetry parameter,  $g$ , which is quite uncertain for ice clouds. Therefore, it is important to report not only cloud optical thickness  $\tau$  but also the retrieved transport optical thickness  $\tau_{\text{tr}} = (1-g)\tau$  in the output of cloud retrieval algorithms.

### 5.2.4 Effective Radius

The effective radius,  $a_{\text{ef}}$ , for a spherical polydisperse distribution in a cloud is defined as the ratio of the third to the second moment of the size distribution.

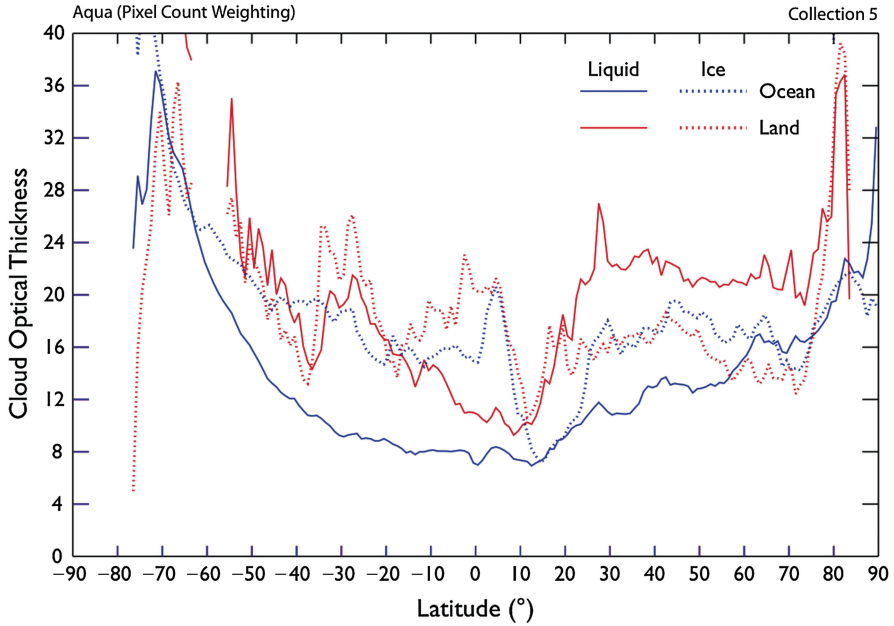


**Fig. 5.6** Zonal mean monthly cloud optical thickness (separated by phase, land, and ocean) derived from the MODIS Aqua cloud optical properties product for April 2005.

For non-spherical ice particles, it is defined as the ratio of three times the average volume  $V$  to the average surface area  $S$  of crystals, i.e.

$$a_{ef} = \frac{3V}{S}, \quad (5.7)$$

which is equivalent to the definition for spherical particles. The determination of  $a_{ef}$  from satellite measurements for spherical water droplets is straightforward. LUTs of reflection functions for two channels, e.g. positioned at 670 and 1600 nm, are calculated and then used simultaneously to retrieve both the effective radius and optical thickness that best match the corresponding measurements. It must be emphasised that *a priori* assumptions about the shape of crystals are needed for ice clouds in order to derive their sizes.

The value of the effective radius is determined mostly from light absorption in a near infrared channel (larger particles with larger absorption and smaller reflectance), whereas information about cloud optical thickness comes primarily from the measurements in a non-absorbing visible or shorter wavelength near-infrared channel (Arking and Childs 1985; Twomey and Cocks 1989; Nakajima and King 1990; Nakajima et al. 1991; Han et al. 1994; Platnick et al. 2001). The exclusion is the use of the rainbow feature to extract the value of  $a_{ef}$ . Then actually not absorption but scattering processes are used for the effective radius determination. Cloud-bows are more easily observed in the angular patterns of the polarized reflectance. This fact

was used by Bréon and Goloub (1998) for the cloud droplet sizing based on POLDER measurements.

Generally,  $a_{ef}$  increases towards the bottom of ice clouds. It decreases towards the bottom for liquid water clouds. As electromagnetic radiation of different wavelengths penetrates to different depths inside the cloud, the retrieved value of  $a_{ef}$  varies with height and depends on wavelength,  $\lambda$ . Typically measurements in the 1.6 and 2.1  $\mu\text{m}$  bands, which are almost free of gaseous absorption, are used in retrievals of the effective radius of droplets or crystals.

For the case of ice clouds having large crystals, one can also use the reflection function at 1.2  $\mu\text{m}$  for the retrievals of  $a_{ef}$ . Then the light absorption is quite small and the simplified version of the asymptotic radiative transfer theory, valid assuming that single scattering albedo  $\omega_0 \rightarrow 1$ , is used in the retrieval procedures (Kokhanovsky et al. 2003; Kokhanovsky 2006).

The reflection function in absorbing near-infrared channels reaches a limiting value with increasing  $\tau$  relatively quickly, when compared to the non-absorbing visible channels. The following approximation for the reflection function of a semi-infinite absorbing layer is then used (Kokhanovsky et al. 2003):

$$R_\infty(\mu, \mu_0, \varphi) = R_{0\infty}(\mu, \mu_0, \varphi) \exp[-4sQ(\mu, \mu_0, \varphi)], \quad (5.8)$$

where  $R_{0\infty}(\mu, \mu_0, \varphi)$  is the reflection function of a non-absorbing semi-infinite layer,

$$Q(\mu, \mu_0, \varphi) = \frac{K_0(\mu)K(\mu)}{R_{0\infty}(\mu, \mu_0, \varphi)}, \quad (5.9)$$

$$s = \sqrt{\frac{1 - \omega_0}{3(1 - \omega_0 g)}}. \quad (5.10)$$

It follows from Eq. 5.8:

$$s = \frac{\ln(R_{0\infty}/R)}{4Q}. \quad (5.11)$$

The parameter  $s$  can be also derived from Mie theory for water droplets and from geometrical optics calculations for large ice crystals. It depends on the effective radius because it follows:

$$1 - \omega_0 \sim \kappa a_{ef}, \quad s \sim \sqrt{\kappa a_{ef}}, \quad \kappa = 4\pi\chi/\lambda \quad (5.12)$$

where  $\chi$  is the imaginary part of the refractive index of a particle (ice or water). Therefore,  $a_{ef}$  can be determined using the measured value of  $R$  and also LUTs of  $Q$  and  $R_{0\infty}$ . As mentioned, the determination of  $a_{ef}$  for crystalline clouds is not straightforward because the shape (habit) distribution of particles cannot be retrieved from passive satellite measurements (Rolland et al. 2000; King et al. 2004; Ou et al. 2005). *A priori* information on the mixture of shapes in the cloud is

needed, and the retrieval results depend on these *a priori* assumptions. The monthly mean effective radius derived from MODIS data is shown in Fig. 5.7. Radii are in the range 5–25  $\mu\text{m}$  for liquid water droplets and they are somewhat larger (up to 30  $\mu\text{m}$ ) for ice clouds in the region of the ITCZ. The mean latitudinal distribution of the effective radius is given in Fig. 5.8. It follows from this figure that ice particles have larger sizes compared to water droplets. The retrieved sizes of crystals and droplets characterise the microphysical conditions in the upper portion of the cloud, because solar radiation, which is absorbed in the near-infrared, does not penetrate strongly to the lower levels of an optically thick cloud.

It follows from Fig. 5.7 that particles are generally larger over the ocean. This is explained by the fact that less cloud condensation nuclei are available over ocean as compared with clouds over land, but it might also be partially indicative of different dynamic processes above land and ocean. There is a hemispherical asymmetry in the distribution of  $a_{ef}$  (Fig. 5.8). This is related to different areas of land in the northern and southern hemispheres. Droplets in water clouds are generally smaller in the northern latitudes as compared to the southern latitudes. This is consistent with the fact that most industrial activity is in the northern hemisphere, leading to a hemispheric increase in the aerosol particle numbers and, as a consequence, a decrease in droplet sizes and precipitation probabilities. However this hemispheric feature is absent for ice clouds.

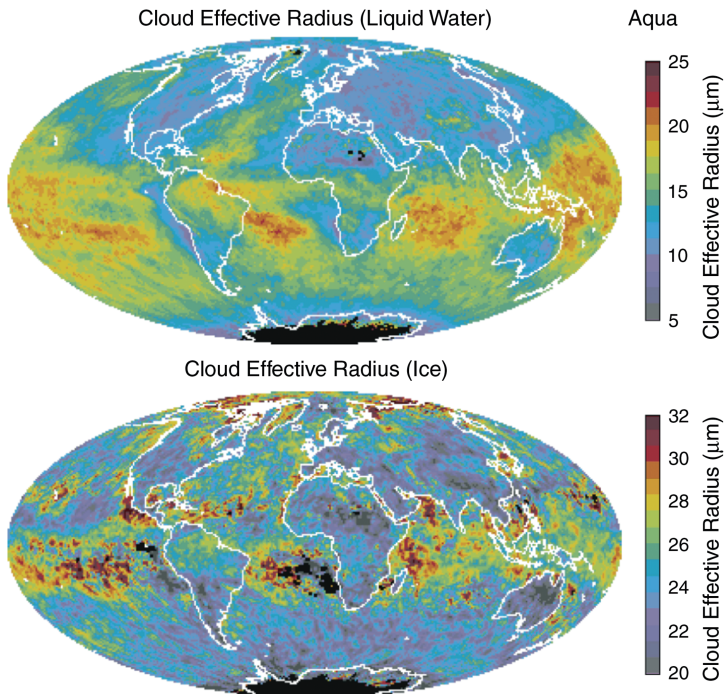


**Fig. 5.7** The monthly mean effective radius of water droplets and ice crystals (April 2005, MODIS Aqua).

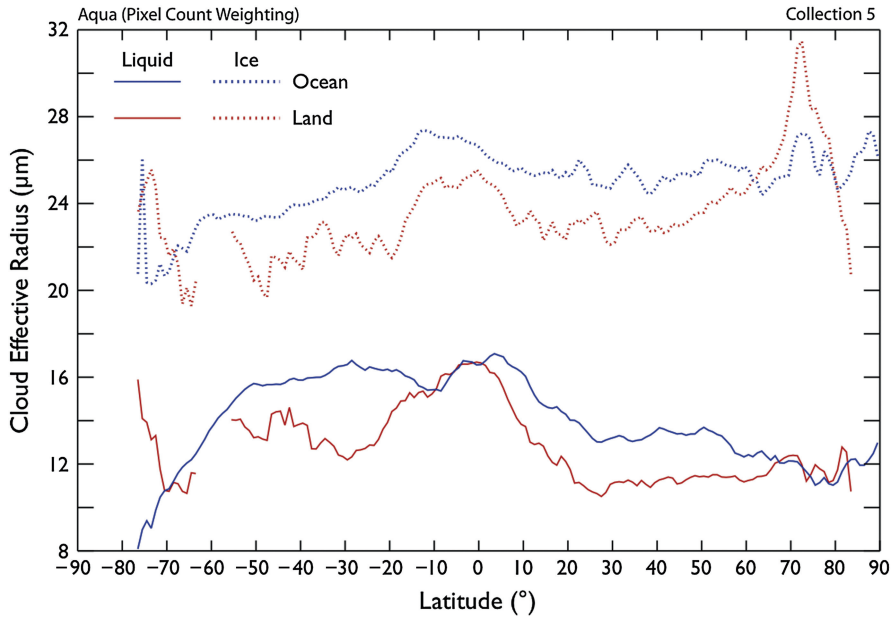


Fig. 5.8 The latitudinal distribution of cloud effective radius (April 2005, MODIS Aqua).

### 5.2.5 Cloud Liquid Water and Ice Path

As described in the previous chapter on microwave remote sensing, the liquid water path is an important parameter for clouds, which can be determined in different spectral regions from the absorption of liquid water. The amount of liquid water mass in a vertical cloud column of a unit area, or liquid water path, LWP, is calculated from the following equation:

$$LWP = \rho \int_0^L C_v(z) dz, \tag{5.13}$$

Where  $\rho$  is the density of liquid water,  $L$  is the geometrical thickness of the cloud and  $C_v$  is the dimensionless volumetric concentration of water in the cloud. For a vertically homogeneous cloud, it follows:

$$LWP = \rho C_v L. \tag{5.14}$$

LWP is typically measured in  $g/m^2$  and usually lies in the range 50–200  $g/m^2$ . The value of the LWP is retrieved from the measured values of  $a_{ef}$  and  $\tau$ , explained

above. It follows for an idealized vertically homogeneous cloud with large particles ( $a_{ef} \gg \lambda$ ):

$$\tau = NSL/2 \quad (5.15)$$

where  $S$  is the average surface area of the particles in a cloud and  $N$  is the number of particles in a unit volume, which is related to the volumetric concentration *via* the following equation:

$$N = \frac{C_v}{V}. \quad (5.16)$$

It follows from Eqs. 5.15, 5.16 and 5.14:

$$\tau = \frac{3LWP}{2\rho a_{ef}}, \quad (5.17)$$

and, therefore,

$$LWP = \frac{2}{3}\rho a_{ef}\tau. \quad (5.18)$$

This equation yields LWP from measurements of  $a_{ef}$  and  $\tau$ . Eq. 5.17 is also used for the determination of the ice water path, IWP, defined via Eq. 5.12 with  $\rho$  as the density of ice and  $C_v$  as the dimensionless volumetric concentration of ice in the cloud. In this case all parameters in Eq. 5.18 are referred to ice (e.g. ice density  $\rho$  and effective size of ice grains  $a_{ef}$ ).

The LWP cannot be determined from measurements in the visible and near-infrared for thick clouds because the reflection function becomes insensitive to the cloud optical thickness, as the electromagnetic radiation does not penetrate sufficiently into the cloud. For such clouds, the microwave measurements must be used as described in Chapter 4. The global distribution of the LWP as determined from MODIS is shown in Fig. 5.9. Large values of LWP are characteristic for polar regions. Further discussion of MODIS cloud products is provided by Platnick et al. 2003 and references therein.

## 5.2.6 Cloud Top Height

Cloud altitude and type are associated with the thermodynamic and hydrodynamic structure of the atmosphere and affect the energy budget and the radiative heating profile. Therefore, it is important to monitor cloud top height (CTH) statistics with

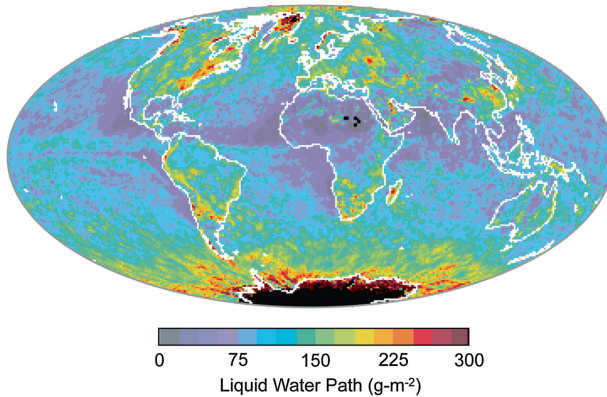


**Fig. 5.9** The global distribution of LWP for April 2005 derived from the MODIS Aqua optical property retrievals.

satellite measurements. Several passive techniques have been developed for this purpose, including:

- Stereoscopy,
- Thermal infrared measurements,
- Gaseous absorption measurements.

In the stereoscopic method (Moroney et al. 2002), a cloud is observed from different view angles so enabling the detection of its height from parallax considerations.

The thermal infrared measurements are based either on measurements of brightness temperature at 11 or 12  $\mu\text{m}$ , for example, with colder clouds being higher in atmosphere, and/or  $\text{CO}_2$  slicing techniques, which use measurements in the  $\text{CO}_2$  absorption bands around 14–15  $\mu\text{m}$  (Strabala et al. 1994; Rossow and Schiffer 1999).

The  $\text{CO}_2$  slicing technique assumes that the atmosphere becomes more opaque as the wavelength increases from 13.3 to 15  $\mu\text{m}$ : the radiances obtained from these spectral bands being sensitive to different layers in the atmosphere (Menzel et al. 2008). The cloud top heights (or pressures) data products, determined from MODIS data, use the  $\text{CO}_2$  slicing method applied to three channels (13.64, 13.94 and 14.24  $\mu\text{m}$ ). As a result of its signal-to-noise range, MODIS  $\text{CO}_2$  slicing cloud-top pressures are typically limited to pressures from approximately 700 hPa (about 3 km above sea level) up to the tropopause. Consequently, when low-level clouds are present, the MODIS CTH algorithm defers to an infrared window technique where cloud-top pressure and temperature are determined through comparison of model-calculated and observed 11  $\mu\text{m}$  radiances.

Solar reflectance measurements in the oxygen absorption bands, e.g. A, B,  $\gamma$  and also the absorption band of the molecular complex ( $\text{O}_2\text{-O}_2$ ), have often been used to determine cloud top height (Hanel 1961; Yamamoto and Wark 1961;

Saiedy et al. 1965; 1967; Heidinger and Stephens 2000; Koелеmeijer et al. 2001; Rozanov and Kokhanovsky 2004). The first CTH satellite measurements using the O<sub>2</sub> A-band were made by astronauts aboard the Gemini satellite in the 1960s (Saiedy et al. 1965; 1967). The technique is similar to that of CO<sub>2</sub> slicing in the sense that the sensitivity to cloud layers depends on absorption of a well-mixed gas (e.g. the O<sub>2</sub> A-band absorption increasing from 758 to 761 nm). Hyper-spectral measurements are needed because the absorption process takes place in a narrow spectral region. The physical principle behind the technique is demonstrated in Fig. 5.10, where calculations of the reflection function at different CTHs in the oxygen A-band are presented. Higher clouds give shallower spectra. The fit of the measured spectra in the oxygen absorption bands (A, B, or  $\gamma$ ) enables the CTH to be determined with  $a_{ef}$  and  $\tau$ , and cloud phase determined from other channels almost free of the gaseous absorption.

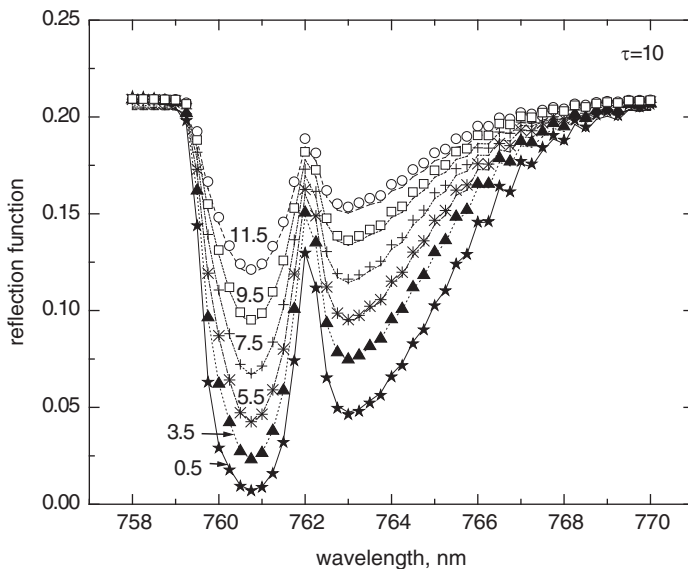


**Fig. 5.10** Dependence of the cloud reflection function on the wavelength in the oxygen A-band for cloud top heights equal to 0.5, 3.5, 5.5, 7.5, 9.5, 11.5 km at the cloud optical thickness  $\tau = 10$  and  $a_{ef} = 6 \mu\text{m}$  (the Deirmendjian's Cloud C1 model). The cloud geometrical thickness is equal to 250 m. The solar zenith angle is  $60^\circ$  and the observations are performed along the vertical to the scattering layer. Lines are plotted using the simplified asymptotic radiative transfer theory applied to the calculation in the O<sub>2</sub> A-band (Kokhanovsky, 2006). Symbols give results of the exact radiative transfer calculations.

The technique appears to work quite well for low and middle level clouds using relatively poor spectral resolution data. Such data are relatively insensitive to thin cirrus and further development work is being undertaken to improve these retrievals. The observation of large differences between CTH derived from IR and O<sub>2</sub> absorption techniques is used to identify multi-layered clouds. The difference can be

explained by the different sensitivities of the emitted thermal IR and the backscattered solar light to CTH. So the techniques are quite complimentary to each other.

For the mapping from cloud pressure (hPa) to cloud top height (km) and back, a climatology of pressure vertical profiles are needed. The profiles will vary to some extent depending on the location and season but, to a good approximation, is given by the following simple expression:

$$p = p_0 \exp(-z/H), \quad (5.18)$$

where  $H$  is the scale height,  $z$  is the height above the ground,  $p$  is the atmospheric pressure at the level  $z$ , and  $p_0$  is the pressure at the ground level. The MODIS global mean cloud top pressure for May 2008 is shown in Fig. 5.11.

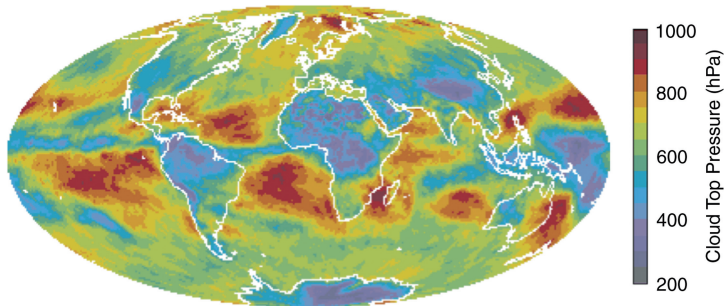


**Fig. 5.11** Global mean cloud top pressure derived from MODIS Aqua observations for April 2005.

### 5.3 Validation of Satellite Cloud Products

The validation of satellite-derived cloud products is essential to establish the accuracy of the data products. Long-term ground and/or airborne measurements are needed in order to have statistically significant results for clouds of different types. Ideally, the most direct measurement of the cloud parameter of interest is desired. This requires diverse instrumentation ranging from particle size spectrometers to lidars and radars. Most importantly, the uncertainties of the validating instruments must be known in order to assess satellite retrieval uncertainties.

As an example, cloud top heights can be determined from ground-based, airborne or satellite lidars and radars (each with different height sensitivities) and compared to CTHs derived from the passive instruments. A difficulty here is that of the averaging scale. Lidars and radars provide information at a given spatial location (ground-based systems) or along thin curtains (CALIPSO and CloudSat). Satellite imagers give information from pixels typically of  $1 \text{ km}^2$  in size. Therefore, comparisons are meaningful only when passive and active satellite data can be spatially sampled or averaged in a commensurate manner, and ground-based active systems data are appropriately averaged in time. Fig. 5.12 shows comparisons of

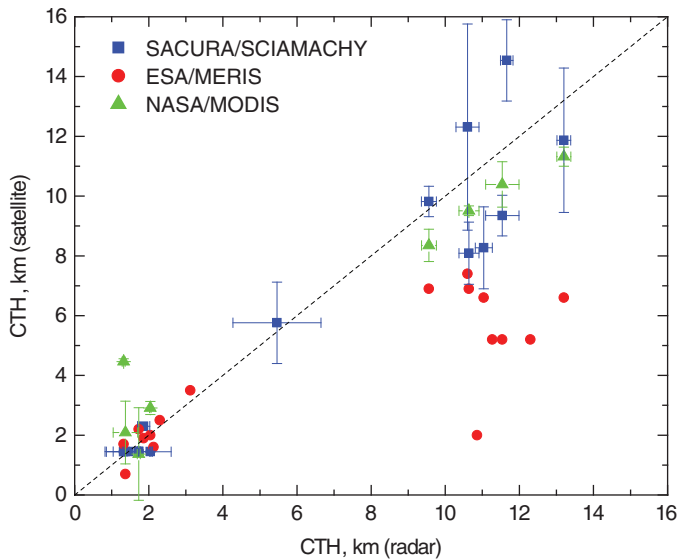


**Fig. 5.12** Inter-comparison of ground-radar (35 GHz) and satellite cloud top heights for overcast scenes at the Southern Great Plains (SGP) ARM site (Kokhanovsky et al. 2008).

cloud top heights derived from the 35 GHz MMCR ground radar measurements and official products from NASA (MODIS Collection 5), ESA (MERIS), and the University of Bremen (UB; SCIAMACHY). The oxygen A-band technique is used for the ESA and UB products. The CO<sub>2</sub> slicing (high clouds) and thermal infrared (low clouds) are used in the MODIS CTH product. The comparisons have been performed for the time period 2002–2007. Only those dates when all instruments operated simultaneously and there were extended cloud fields over the site were used in the intercomparison study.

While lidars and radars provide direct information on the cloud top height, their CTHs may differ somewhat due to the different sensitivities of these systems to particles of different sizes and composition. The radar is known to be less sensitive than a lidar to boundaries in low extinction clouds (e.g. lower heights relative to lidar for cirrus clouds, or perhaps missing the cirrus entirely). Further, techniques using different parts of the spectrum have different penetrations into the cloud and thus the definition of cloud top can be ambiguous. With these caveats, Fig. 5.12 shows that low-level cloud heights from MERIS, MODIS and SCIAMACHY UB (SACURA algorithm) are very close to the radar values. However, there are some problems with respect to high clouds where MODIS heights are lower than the radar and MERIS CTHs are even lower. The SCIAMACHY cloud product shows large differences for high clouds although the overall bias relative to the radar is small.

Shortcomings of the current generation of MERIS CTH retrievals are due to the fact that the instrument does not have thermal infrared channels and the measurement in the oxygen A-band is made with one broadband spectral channel. In contrast, SCIAMACHY performs hyperspectral measurements (with the spectral resolution

of 0.54 nm) in the oxygen A-band while MODIS has a number of thermal infrared channels that increases the accuracy of the corresponding retrieval algorithms.

Infrared techniques are very sensitive to high cirrus clouds, but this is not the case for oxygen A-band spectrometry. Therefore, the combination of both types of measurements must be used to increase the retrieval information content such as various cloud top definitions, the identification of multi-layered cloud systems, the cloud bottom height determination, etc.

As previously mentioned, the cloud fraction depends on the spatial resolution of the satellite imager. The retrievals of cloud effective radius and cloud phase can be compared with airborne measurements. However, differences between the satellite-derived effective radius and that measured in the cloud may not necessarily be due to algorithm errors but could also include *in situ* sampling errors from an inhomogeneous cloud. The uncertainties in the size distributions obtained from these probes are usually unspecified, especially for ice particles and water droplets in drizzling clouds.

Independent cloud optical thickness and liquid water path measurements, say from ground-based radiometers ( $\tau$ ) and radars (LWP), do not necessarily give unbiased retrievals any more than the satellite retrievals do. For example, radars are less sensitive to small particles and, therefore, the radar-derived LWP can differ from that derived from a satellite optical instrument when size distribution assumptions used in the radar retrieval are incorrect. Ground-based radiometers cannot measure directly transmitted radiation for thick clouds, but rather the transmitted diffuse light from which cloud optical thickness is derived. However, sampling volume problems can once again be important.

As one can conclude, there is an urgent need to develop additional cloud product validation techniques (instrumentation and/or algorithms). Inter-comparisons of products derived from different approaches (whether satellite, ground-based, or aircraft) for the same cloud system must be performed; diverse results serve as an indication of problems in one or more of the techniques.

## 5.4 Modern Trends in Optical Cloud Remote Sensing from Space

### 5.4.1 Hyperspectral Remote Sensing

The traditional studies of cloud properties have been performed using the channels positioned at 0.65 (0.865), 1.6, and 12  $\mu\text{m}$ . This enables the determination of cloud liquid water path, the size of droplets/crystals, the cloud optical thickness and also the cloud altitude. However, in recent years, hyper-spectral remote sensing of clouds becomes more and more popular. Unlike traditional methods, where the reflected radiation is measured in quite broad spectral channels (10 nm and even wider), hyper-spectral remote sensing, with a spectral resolution of about a nanometer, offers much more detailed spectral information. SCIAMACHY for example

has a resolution of 0.2–1.5 nm. The corresponding retrieval methods are poorly developed at the moment. However, the potential of hyper spectral remote sensing in the vertical profiling of clouds cannot be underestimated. Indeed, the penetration depth of radiation depends on the wavelength. Therefore, the spectral scanning of reflected radiation in the range 0.4–2.2  $\mu\text{m}$  can bring information on the vertical distribution of cloud properties such as the liquid water content and the size of particles. Also positions of cloud boundaries can be found. Corresponding methods are not mature enough. But several important results have been obtained.

The depth of solar Fraunhofer lines in scattered light is less than that observed in the direct sunlight. This is called the Ring effect. The physical mechanism behind this effect is clear: it is largely due to rotational Raman scattering from the wings of the absorption line towards its center. Due to gaseous absorption effects Raman scattering from the centre of the band to the wings is much less pronounced than in the wings→band centre processes, which leads to the filling-in of the gaseous absorption features in the terrestrial atmosphere. De Beek et al. (2001) used Ring effect for the Ca II Ring structure at 393.37 nm to get the cloud top height and also cloud optical thickness (COT) from GOME measurements in the spectral range 392–395 nm. They demonstrated using the software package SCIATRAN that the filling-in decreases with the COT and also with the CTH. The effect of increasing COT and CTH on filling-in of Ca II absorption line is quite obvious: clearly, clouds shield lower atmospheric layers, which reduces molecular scattering events and their Raman scattering contributions. To increase the accuracy of retrievals, the authors also used the measurements in the absorption bands of  $\text{O}_2\text{--O}_2$  (477 nm) and  $\text{O}_2$  (761 nm). Some earlier results in this area have been obtained by Brinkman (1968), Wallace (1972), Price (1977), Park et al. (1986) and Joiner and Bhartia (1995). Comprehensive radiative transfer models of rotational Raman scattering (for forward and inverse modelling) were developed by van Deelen (2007). Joiner and Vasilkov (2006) applied the technique to OMI data. The use of measurements inside gaseous absorption bands (e.g.  $\text{O}_2$ ,  $\text{CO}_2$ ) were used for a long time to get the cloud top altitudes. Saiedy et al. (1965; 1967) reported measurements in  $\text{O}_2$  A-band using a hand held spectrometer from a satellite. More recently, the GOME and SCIAMACHY  $\text{O}_2$  A-band measurements have been used for the same task by Kuze and Chance (1994), Koелеmeijer et al. (2001), Loyola (2004), Rozanov and Kokhanovsky (2004), Grzegorski et al. (2006), Rozanov et al. (2006), Kokhanovsky et al. (2007), van Diedenhoven (2007) and van Diedenhoven et al. (2007). In the last paper the synergetic UV and  $\text{O}_2$  A-band measurements have been used to deduce the cloud properties. It is known that clouds screen gaseous atmosphere beneath them, leading to less sharp increase of the top-of-atmosphere reflectance in the UV (Herman et al. 2001). This effect is used for the improvement of the cloud top altitude retrieval algorithm based on  $\text{O}_2$  A-band measurements.  $\text{CO}_2$  molecular absorption band centered around 14  $\mu\text{m}$  is routinely used for the MODIS CTH determination (Menzel et al. 2008).

SACURA cloud top height retrieval algorithm (Rozanov and Kokhanovsky 2004) is based on the asymptotic radiative transfer theory generalized on the case of gaseous absorption in a vertically inhomogeneous cloud. Therefore, it provides

not effective but the true cloud top heights as demonstrated in the previous section (see Fig. 5.12). Other cloud top height retrieval algorithms (e.g. FRESKO (Koelemeijer et al. 2001), ROCINN (Loyola 2004)) are based on the substitution of a cloud by a Lambertian cloud, which brings some biases in the retrieved cloud top heights (usually too low clouds are retrieved). A comprehensive study of various approximations usually applied in cloud top height retrievals using oxygen A-band have been performed by Rozanov and Kokhanovsky (2008).

### 5.4.2 Lidar Remote Sensing

Active systems for cloud remote sensing from space have quite a short history. There were only three missions up to date:

- Lidar In-space Technology Experiment (LITE, <http://www-lite.larc.nasa.gov/>, 1994),
- Geoscience Laser Altimeter System (GLAS, <http://glas.gsfc.nasa.gov/>, 2003–2008), and
- The Cloud-Aerosol Lidar and Infrared Pathfinder Satellite Observation (CALIPSO) satellite mission (<http://www-calipso.larc.nasa.gov/>, 2006–present) with a lidar system called CALIOP.

The LITE instrument was powered continuously for over 220 h during the mission, with 53 h of lasing at wavelengths 355, 532, and 1064 nm (Winker et al. 1996). LITE unambiguously sensed sub-visible cirrus and has provided a global look at the prevalence and height of very thin clouds that are below the threshold of detection of current passive satellite instruments. Even deep cirrus was generally fully penetrated, so that the vertical structure of the clouds could be observed, and the presence of underlying cloud layers detected. Theoretical results related to LITE were reported by Winker and Poole (1995). Zege et al. (1995) developed an analytical method for the calculation of lidar returns from clouds both from ground and space.

GLAS was successfully launched aboard the ICESat, from Vandenberg Air Force Base, California on 12th January 2003. At an altitude of approximately 600 km, GLAS provides global coverage between 86°N and 86°S. The GLAS laser transmits short pulses (4 nanoseconds) of infrared light at 1064 nm and visible green light at 532 nm 40 times per second. The spatial resolution of the disk illuminated by the laser is 70 m in diameter and spaced at 170 m intervals along the Earth's surface. Many investigations of cloud systems using GLAS have been performed. In particular, Dessler et al. (2006) analyzed cloud-top height data obtained at tropical latitudes between 29th September and 17th November 2003. They found that about 66% of the tropical observations show one or more cloud layers. Of those observations that do show a cloud, about half show two or more cloud layers. Maxima in the cloud-top height distribution occur in the upper troposphere, between 12 and 17 km, and in the lower troposphere, below about 4 km. A less prominent maximum occurs in the mid-troposphere, between 6 and 8 km. The occurrence of cloud layers tends to be consistent with the well known diurnal cycles of continental and oceanic convection, and it was found that cloud layers tend to occur more frequently over land than over ocean, except in the lower

troposphere, where the opposite is true. Wang and Dessler (2006) used GLAS measurements to establish the cloud overlap statistics in the tropical area.

The Cloud–Aerosol Lidar and Infrared Pathfinder Satellite Observation satellite mission carries an active lidar (CALIOP with channels at 532 nm (with the depolarization measurements) and 1064 nm), a passive Infrared Imaging Radiometer (IIR), and visible Wide Field Camera. By deriving accurate statistics on cloud height and structure, CALIOP since its launch on 28th April 2006 provided valuable statistical data – especially with respect to thin clouds such as  $C_i$  and sub-visual  $C_i$  not seen by passive radiometers. In particular, Sassen et al. (2008) derived valuable information on the global distribution of cirrus clouds. The latitudinal distribution of identified cirrus cloud heights derived for 0.2 km and 2.5° grid intervals is shown in Fig. 5.13. As one may expect both the frequency of  $C_i$  cloud occurrence and also their altitudes increase towards the equator.

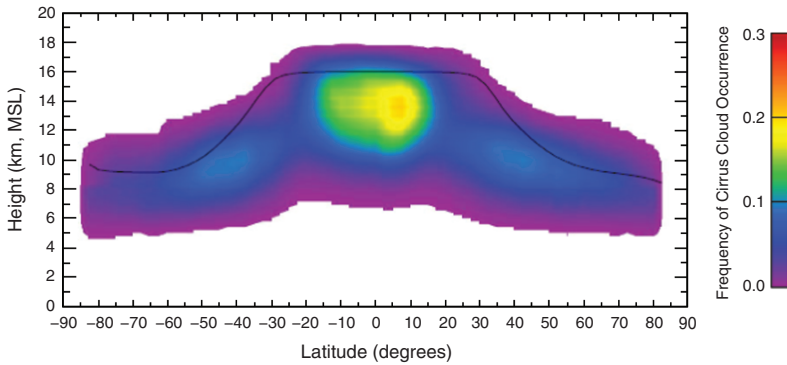


**Fig. 5.13** Latitudinal distribution of identified cirrus cloud heights derived for 0.2 km height and grid 2.5° intervals. The line shows the mean tropopause heights averaged over the same one year period, as taken from CALIPSO data files (from Sassen et al. (2008)).

The study of clouds using synergy of lidar and radar (CloudSat, Stephens et al. (2008)) systems in space is also a hot topic in modern satellite cloud remote sensing from space (Barker 2008; Grenier et al. 2009; Haladay and Stephens 2009; Mace et al. 2009; Wu et al. 2009). Clearly, the synergy of multiple satellite systems (including those on a geostationary orbit) will enhance our detailed understanding of the terrestrial cloud system and also on a scale unavailable in the past. This will contribute appreciably to our progress in understanding the terrestrial atmosphere, weather, and climate.

### 5.4.3 Future Missions

Satellite remote sensing of clouds will be continued through a number of missions planned by space agencies worldwide.

*NPP (NASA)*. The National Polar orbiting Operational Environmental Satellite System Preparatory Project will be launched in 2011.

- CrIS: The Cross-track Infrared Sounder will be combined with the Advanced Technology Microwave Sounder (ATMS). They produce atmospheric temperature, moisture and pressure profiles from space.
- OMPS: Ozone Mapping and Profiler Suite.
- VIIRS: Visible/Infrared Imager/Radiometer Suite collects visible and infrared radiometric data of the Earth's atmosphere, ocean, and land surfaces. Data types include atmospheric aerosols and clouds, land cover and reflectance, land/water and sea surface temperature, ocean color, and low light imagery.
- CERES: Earth's Radiant Energy System.

*SENTINEL 3 (ESA)*. This mission will be launched in 2012.

- A topography system, which includes a dual-band Ku- and C-band altimeter based on technologies used on ESA's Earth Explorer CryoSat mission, a microwave radiometer for atmospheric correction and a DORIS receiver for orbit positioning.
- An Ocean Land Colour Instrument (OLCI), which is based on heritage from ENVISAT's Medium Resolution Imaging Spectrometer MERIS instrument. The OLCI operates across 21 wavelength bands from ultraviolet to near-infrared and uses optimised pointing to reduce the effects of sun glint.
- A surface temperature system called Sea Land Surface Temperature Radiometer (SLSTR), which is based on heritage from ENVISAT's Advanced Along Track Scanning Radiometer (AATSR). The SLSTR uses a dual viewing technique and operates across eight wavelength bands providing better coverage than AATSR because of a wider swath width.

*EARTHCARE(ESA)*. The mission will be launched in 2013.

- Backscatter Lidar (ATLID)
- Cloud Profiling Radar (CPR),
- Multi-Spectral Imager (MSI), 7 channels, 150 km swath, 500 m pixel,
- Broadband Radiometer (BBR) – 2 channels, 3 views (nadir, fore and aft),

*GCOM-C (JAXA)*. This mission will be launched in 2014.

- Second-Generation Global Imager (S-GLI). The spectral coverage is 0.375–12.5  $\mu\text{m}$  in 19 spectral bands with the spatial resolution 0.25–1 km depending on the band.

The instrument set-up is similar in many respects to MODIS and can be used for the droplet to crystal size monitoring and also for the determination of the cloud top height, cloud phase, cloud optical thickness, liquid water path and other relevant cloud parameters. In addition, the instrument has a capability of measuring the polarization state of the reflected light. Measurements in the oxygen A-band are also planned.

## 5.5 Conclusions

Our need to understand the hydrological cycle is driven by scientific curiosity, the operational requirements for numerical weather prediction and, in the future, climate change. Many instruments and fruitful retrieval techniques have been developed and applied to satellite data to derive cloud data products. The wealth of detailed cloud property information that has been obtained and understood on a global scale would have been impossible before the satellite era. However, to meet the evolving scientific and societal issues related to numerical weather prediction and climate change, many problems still remain to be solved. These address improved missions that are fit for purpose together with algorithm development. They are mostly related to the adequacy of the forward models used in the retrieval algorithms. Until now, all operational cloud retrieval algorithms rely on a homogeneous, single-layered cloud model. In reality, clouds are inhomogeneous objects on all scales in the horizontal and the vertical. 3-D effects are ignored in cloud satellite remote sensing as look-up-tables are calculated using 1-D radiative transfer theory. Therefore, retrievals can be biased for cases where 3-D effects are pronounced, such as scattered cloud fields and extensive vertical convection. Further issues exist for studies of thin clouds, where both cloud inhomogeneity, cloud fraction, and the underlying surface bi-directional reflectance function must be accounted for in the retrieval process. The retrievals of ice clouds rely on the *a priori* assumed models of crystal shapes, which may vary with other cloud microphysical parameters for a given location and time. Again, this leads to biases in the derived products. The retrievals of mixed phase cloud properties such as the ice/water fraction are not yet well developed. However, hyper-spectral measurements show some potential in this respect. The exploration of these important retrieval issues will lead the list of important tasks needed to advance cloud satellite remote sensing in the coming years.

**Acknowledgements** The authors are grateful to the members of their research groups for the support, advice, and preparation of figures used this work. The support of ACCENT and editors of this book is much appreciated. The use of ESA, NASA and ARM SGP radar data is acknowledged with many thanks.

## References

- Ackerman, S., K. Strabala, W. Menzel, R. Frey, C. Moeller, and L. Gumley, 1998, Discriminating clear sky from clouds with MODIS. *J. Geophys. Res.*, **103**, 32141–32157.
- Arking, A., and J. D. Childs, 1985, Retrieval of cloud cover parameters from multispectral satellite images, *J. Appl. Meteorol.*, **24**, 323–333.
- Barker, H. W., 2008, Overlap of fractional cloud for radiation calculations in GCMs: A global analysis using CloudSat and CALIPSO data, *J. Geophys. Res.*, **113**, doi:10.1029/2007JD009677.
- Baum, B. A., P. F. Soulen, K. I. Strabala, M. D. King, S. A. Ackerman, W. P. Menzel, and P. Yang, 2000, Remote sensing of cloud properties using MODIS airborne simulator imagery during SUCCESS. II. Cloud thermodynamic phase. *J. Geophys. Res.*, **105**, 11781–11792.

- Bréon, F., and P. Goloub, 1998, Cloud droplet effective radius from spaceborne polarization measurements, *Geophys. Res. Lett.*, **25**, 1879–1882.
- Brinkman, R. T., 1968, Rotational Raman scattering in planetary atmospheres, *Astrophys. J.*, **15**, 1087–1093.
- de Beek, R., M. Vountas, V. V. Rozanov, A. Richter, and J. P. Burrows, 2001, The ring effect in the cloudy atmosphere, *Geophys. Res. Lett.*, **28**, 721–724.
- Dessler, A. E., S. P. Palm, and J. D. Spinhirne, 2006, Tropical cloud-top height distributions revealed by the Ice, Cloud, and Land Elevation Satellite (ICESat)/Geoscience Laser Altimeter System (GLAS), *J. Geophys. Res.*, **111**, D12215, doi:10.1029/2005JD006705.
- Goloub, P., M. Herman, H. Chepfer, J. Riedi, G. Brogniez, P. Couvert, and G. Sèze, 2000, Cloud thermodynamical phase classification from the POLDER spaceborne instrument, *J. Geophys. Res.*, **105**, 14747–14759.
- Grenier, P., J. Blanchet, and R. Muñoz-Alpizar, 2009, Study of polar thin ice clouds and aerosols seen by CloudSat and CALIPSO during midwinter 2007, *J. Geophys. Res.*, **114**, D09201, doi:10.1029/2008JD010927.
- Grzegorski, M., M. Wenig, U. Platt, P. Stammes, N. Fournier, and T. Wagner, 2006, The Heidelberg iterative cloud retrieval utilities (HICRU) and its application to GOME data, *Atmos. Chem. Phys.*, **6**, 4461–4476.
- Haladay, T., and G. Stephens, 2009, Characteristics of tropical thin cirrus clouds deduced from joint CloudSat and CALIPSO observations, *J. Geophys. Res.*, **114**, doi:10.1029/2008JD010675.
- Han, Q., W. B. Rossow, and A. Lacis, 1994, Near-global survey of effective droplet radius in liquid water clouds using ISCCP data, *J. Climate*, **7**, 465–497.
- Hanel, R. A., 1961, Determination of cloud altitude from a satellite, *J. Geophys. Res.*, **66**, 1300–1300.
- Heidinger, A. K., and G. L. Stephens, 2000, Molecular line absorption in a scattering atmosphere. Part II: Application to remote sensing in O<sub>2</sub> A-band, *J. Atmos. Sci.*, **57**, 1615–1634.
- Herman, J. R., D. Larko, E. Celarier, and J. Ziemke, 2001, Changes in the Earth's UV reflectivity from the surface, clouds, and aerosols, *J. Geophys. Res.*, **106**, 5353–5368.
- Joiner, J., and P. Bhartia, 1995, The determination of cloud pressures from rotational Raman scattering in satellite backscatter ultraviolet measurements, *J. Geophys. Res.*, **100**, 23019–23026.
- Joiner, J., and A. P. Vasilkov, 2006, First results from the OMI rotational Raman scattering cloud pressure algorithm, *IEEE Trans. Geosci. Remote Sens.*, **44**, 1272–1282.
- King, M. D., 1987, Determination of the scaled optical thickness of clouds from reflected solar radiation measurements, *J. Atmos. Sci.*, **44**, 1734–1751.
- King, M. D., S. Platnick, P. Yang, G. T. Arnold, M. A. Gray, J. C. Riedi, S. A. Ackerman, and K. N. Liou, 2004, Remote sensing of liquid water and ice cloud optical thickness, and effective radius in the arctic: Application of airborne multispectral MAS data, *J. Atmos. Oceanic Technol.*, **21**, 857–875.
- Koelemeijer, R. B. A., P. Stammes, J. W. Hovenier, and J. F. de Haan, 2001, A fast method for retrieval of cloud parameters using oxygen A band measurements from the Global Ozone Monitoring Experiment, *J. Geophys. Res.*, **106**, 3475–3490.
- Knap, W. H., P. Stammes, R. B. A. Koelemeijer, 2002, Cloud thermodynamic-phase determination from near-infrared spectra of reflected sunlight, *J. Atmos. Sci.*, **59**, 83–96.
- Kokhanovsky A. A., V. V. Rozanov, E. P. Zege, H. Bovensmann, and J. P. Burrows, 2003, A semianalytical cloud retrieval algorithm using backscattered radiation in 0.4–2.4 μm spectral region, *J. Geophys. Res.*, **108**, doi:10.1029/2001JD001543.
- Kokhanovsky, A. A., 2006, *Cloud Optics*, Dordrecht: Springer.
- Kokhanovsky, A. A., O. Jourdan, and J. P. Burrows, 2006, The cloud phase discrimination from a satellite, *IEEE Geosci. Rem. Sens. Lett.*, **3**, 103–106.
- Kokhanovsky, A. A., M. Vountas, V. V. Rozanov, W. Lotz, H. Bovensmann, and J. P. Burrows, 2007, Global cloud top height and thermodynamic phase distribution as obtained by SCIAMACHY on ENVISAT, *Int. J. Remote Sensing*, **28**, 4499–4507.

- Kokhanovsky, A. A., C. M. Naud, and A. Devasthale, 2008, Inter-comparison of ground-based radar and satellite cloud-top height retrievals for overcast single-layered cloud fields, *IEEE Trans. Geosci. Rem. Sens.*, **47**, 1901–1908.
- Kuze, A., and K. V. Chance, 1994, Analysis of cloud top height and cloud coverage from satellites using the O<sub>2</sub> A and B bands, *J. Geophys. Res.*, **99**, 14,481–14,491.
- Liou, K.-N., 2002, *Introduction to Atmospheric Radiation*, New York: Academic Press.
- Loyola, D.G. R., 2004, Automatic cloud analysis from polar-orbiting satellites using neural network and data fusion techniques, *Proc. Geosci. Remote Sens. Symp.*, **4**, 2530–2533.
- Mace, G. G., Q. Zhang, M. Vaughan, R. Marchand, G. Stephens, C. Trepte, and D. Winker, 2009, A description of hydrometeor layer occurrence statistics derived from the first year of merged CloudSat and CALIPSO data, *J. Geophys. Res.*, **114**, D00A26, doi:10.1029/2007JD009755.
- Menzel, W. P., R. A. Frey, H. Zhang, D. P. Wylie, C. C. Moeller, R. E. Holz, B. Maddux, B. A. Baum, K. I. Strabala, and L. E. Gumley, 2008, MODIS global cloud-top pressure and amount estimation: Algorithm description and results, *J. Appl. Meteor. Climatol.*, **47**, 1175–1198.
- Moroney, C., R. Davies, and J.-P. Muller, 2002, Operational retrieval of cloud-top heights using MISR data, *IEEE Trans. Geosci. Remote Sens.*, **40**, 1532–1546.
- Nakajima, T., and M. D. King, 1990, Determination of the optical thickness and effective particle radius of clouds from reflected solar radiation measurements. Part 1. Theory, *J. Atmos. Sci.*, **47**, 1878–1893.
- Nakajima, T., M. D. King, J. D. Spinhirne, and L. F. Radke, 1991, Determination of the optical thickness and effective particle radius of clouds from reflected solar radiation measurements. Part 2. Marine stratocumulus observations, *J. Atmos. Sci.*, **48**, 782–850.
- Ou, S.C., K. N. Liou, Y. Takano, and R. L. Slonaker, 2005, Remote sensing of cirrus cloud particle size and optical depth using polarimetric sensor measurements, *J. Atmos. Sci.*, **62**, 4371–4383.
- Park H., D. F. Heath, and C. L. Mateer, 1986, Possible application of the Fraunhofer line filling in effect to cloud height measurements, in *Meteorological Optics*, OSA Technical Digest Series, pp. 70–81, Opt. Soc. Am., Washington, D.C.
- Pilewskie, P., and S. Twomey, 1987, Discrimination of ice from water in clouds by optical remote sensing, *Atmos. Res.*, **21**, 113–122.
- Platnick, S., J. Y. Li, M. D. King, H. Gerber, and P. V. Hobbs, 2001, A solar reflectance method for retrieving the optical thickness and droplet size of liquid water clouds over snow and ice surfaces, *J. Geophys. Res.*, **106**, 15185–15199.
- Platnick, S., M. D. King, S. A. Ackerman, W. P. Menzel, B. A. Baum, J. C. Riedi, and R. A. Frey, 2003, The MODIS cloud products: Algorithms and examples from Terra, *IEEE Trans. Geosci. Remote Sens.*, **41**, 459–473.
- Price, M. J., 1977, On probing the outer planets with the Raman effect, *Rev. Geophys.*, **15**, 227–234.
- Rolland, P., K. N. Liou, M. D. King, S. C. Tsay, and G. M. McFarquhar, 2000, Remote sensing of optical and microphysical properties of cirrus clouds using MODIS channels: methodology and sensitivity to assumptions, *J. Geophys. Res.*, **105**, 11,721–11,738.
- Rossow, W. B., and R. A. Schiffer, 1999, Advances in understanding clouds from ISCCP, *Bull. Amer. Meteor. Soc.*, **80**, 2261–2287.
- Rozanov, V. V., and A. A. Kokhanovsky, 2004, The semi-analytical cloud retrieval algorithm as applied to the cloud top altitude and the cloud geometrical thickness determination from the top of atmosphere reflectance measurements in the oxygen absorption bands, *J. Geophys. Res.*, **109**, doi:10.1029/2003JD004104.
- Rozanov, V. V., Kokhanovsky, A. A., D. Loyola, R. Siddans, B. Latter, A. Stevens, and J. P. Burrows, 2006, Intercomparison of cloud top altitudes as derived using GOME and ATSR-2 instruments onboard ERS-2, *Rem. Sens. Environ.*, **102**, 186–193.
- Rozanov V. V. and A. A. Kokhanovsky, 2008, Impact of single- and multi-layered cloudiness on ozone vertical column retrievals using nadir observations of backscattered solar radiation, in: *Light scattering reviews*, (ed. A. A. Kokhanovsky, vol.3), Berlin: Springer-Praxis, 113–190.

- Rozenberg, G. V., M. S. Malkevitch, V. S. Malkova, and V. I. Syachinov, 1978, The determination of optical characteristics of clouds from measurements of the reflected solar radiation using data from the Sputnik "KOSMOS-320", *Izvestiya Acad. Sci. USSR, Phys. Atmos. Okeana*, **10**, 14–24.
- Saiedy, F., Hilleary, D. T., and Morgan, W. A., 1965, Cloud-top altitude measurements from satellites, *Appl. Optics*, **4**, 495–500.
- Saiedy, F. H., H. Jacobowitz, and D.Q. Wark, 1967, On cloud – top determination from Gemini-5, *J. Atmos. Sci.*, **24**, 63–69.
- Sassen, K., Z. Wang, and D. Liu, 2008, Global distribution of cirrus clouds from CloudSat/Cloud-Aerosol Lidar and Infrared Pathfinder Satellite Observations (CALIPSO) measurements, *J. Geophys. Res.*, **113**, doi:10.1029/2008JD009972.
- Schreiner, A.J., D. A. Unger, W. P. Menzel, G. P. Ellrod, K. I. Strabala, and J. L. Pellet, 1993, A comparison of ground and satellite observations of cloud cover, *Bull. Amer. Meteor. Soc.*, **74**, 1851–1861.
- Stephens, G. L., D. G. Vane, S. Tanelli, E. Im, S. Durden, M. Rokey, D. Reinke, P. Partain, G. G. Mace, R. Austin, T. L'Ecuyer, J. Haynes, M. Lebsock, K. Suzuki, D. Waliser, D. Wu, J. Kay, A. Gettelman, Z. Wang, and R. Marchand, 2008, CloudSat mission: Performance and early science after the first year of operation, *J. Geophys. Res.*, **113**, doi:10.1029/2008JD009982.
- Strabala, K. I., S. A. Ackerman, and W. P. Menzel, 1994, Cloud properties inferred from 8–12- $\mu\text{m}$  data. *J. Appl. Meteor.*, **33**, 212–229.
- Twomey, S., and T. Cocks, 1989, Remote sensing of cloud parameters from spectral reflectance in the near-infrared, *Contrib. Atmos. Phys.*, **62**, 172–179.
- van Deelen, R., 2007, Rotational Raman scattering in The Earth's atmosphere, PhD thesis, Free University of Amsterdam.
- van Diedenhoven, B., 2007, Satellite Remote Sensing of Cloud Properties in Support of Trace Gas Retrievals, Ph.D. thesis, Free University, Amsterdam.
- van Diedenhoven, B., O. P. Hasekamp and J. Landgraf, 2007, Retrieval of cloud parameters from satellite-based reflectance measurements in the ultraviolet and the oxygen A-band, *J. Geophys. Res.*, **112**, D15208, doi:10.1029/2006JD008155.
- Wallace, L., 1972, Rayleigh and Raman scattering by H<sub>2</sub> in a planetary atmosphere, *Astrophys. J.*, **176**, 249–257.
- Wang, L., and A. E. Dessler, 2006, Instantaneous cloud overlap statistics in the tropical area revealed by ICESat/GLAS data, *Geophys. Res. Lett.*, **33**, L15804, doi:10.1029/2005GL024350, 2006.
- Winker D. M. and L. R. Poole, 1995, Monte-Carlo calculations of cloud returns for ground-based and space-based LIDARS, *Appl. Phys. B*, **60**, 341–344.
- Winker, D. M., Couch, R. H., and M. P. McCormick, 1996, An overview of LITE: NASA's Lidar In-space Technology Experiment, *Proc. IEEE*, **84**, 164–180.
- Wu, D. L., S. A. Ackerman, R. Davies, D. J. Diner, M. J. Garay, B. H. Kahn, B. C. Maddux, C. M. Moroney, G. L. Stephens, J. P. Veefkind, and M. A. Vaughan, 2009, Vertical distributions and relationships of cloud occurrence frequency as observed by MISR, AIRS, MODIS, OMI, CALIPSO, and CloudSat, *Geophys. Res. Lett.*, **36**, doi:10.1029/2009GL037464.
- Wylie, D., D. L. Jackson, W. P. Menzel, and J. J. Bates, 2005, Trends in global cloud cover in two decades of HIRS observations, *J. Climate*, **18**, 3021–3031.
- Yamamoto, G., and D. Q. Wark, 1961, Discussion of the letter by R. A. Hanel, "Determination of cloud altitude from a satellite", *J. Geophys. Res.*, **66**, 3596–3596.
- Zege, E. P., I. L. Katsev, and I. N. Polonsky, 1995, Analytical solution to LIDAR return signals from clouds with regard to multiple scattering, *Appl. Phys. B*, **60**, 345–353.

